

# Tensile Strained Germanium Microstructures: A Comprehensive Analysis of Thermo-Opto-Mechanical Properties

Costanza Lucia Manganelli,\* Michele Virgilio, Michele Montanari, Ignatii Zaitsev, Nicola Andriolli, Stefano Faralli, Stefano Tirelli, Fabio Dagnano, Wolfgang Matthias Klesse, and Davide Spirito

The influence of the thermomechanical effects on the optical properties of germanium microstructures is investigated. Finite element method (FEM) calculations allow a complete spatial assessment of mechanical deformations induced by a silicon nitride (SiN) stressor layer deposited on Ge micropillars. Simulated strain maps are confirmed by experimental maps obtained by Raman spectroscopy. The theoretical investigation on strain-dependent band structure, including the presence of a strain gradient along the longitudinal direction, is exploited to fully capture photoluminescence spectroscopy experiments. Finally, the joint effect of temperature and strain on the fundamental bandgap is also quantified.

## 1. Introduction

In the last two decades, strain engineering has emerged as a very powerful approach for the enhancement of electronic and optical properties in semiconductors. For example, in-plane electron and hole mobility in silicon (Si) is significantly increased by uniaxial or biaxial stress, boosting the performance of transistors with a technology compatible with standard complementary metal–oxide–semiconductor (CMOS) processing.

In optoelectronics, the strain-induced breaking of crystal centrosymmetry enables optical modulators with improved speed and lower absorption losses. A nonhomogeneous strain on the crystal lattice of Si may induce a second-order susceptibility,<sup>[1]</sup> enabling second-order nonlinear processes (e.g., second harmonic generation)<sup>[2,3]</sup> and enhanced electro-optic modulation without the use of carriers injection.

In parallel, several efforts are going into the realization of light emitters that are fully integrated in Si-based platform, as a cost-effective alternative to III–V materials. Here, the two mayor routes are the use of Ge and its alloys with Si and Sn, and strain engineering. Silicon–germanium–tin (GeSn) alloy can be a promising solution<sup>[4]</sup> because its band structure can be controlled through its composition toward high emission efficiency in a broad spectral range, but these ternary alloys present several technological challenges for the material growth.<sup>[5]</sup> The alternative route for band structure control is the introduction of tensile strain in Ge and GeSn alloys. Here, the target is to exploit tensile strain to reduce the energy barrier between the L and  $\Gamma$  minima of the conduction band, realizing a quasi-direct bandgap material and thus enhancing the radiative efficiency. Moreover, the effect of tensile strain is to remove the degeneracy between heavy hole (HH) and light hole (LH) valence bands and to decrease the energy difference between the conduction and valence bands,<sup>[6,7]</sup> providing the desired control over the bandgap. These band structure effects can be revealed by the photoluminescence (PL) experiments, and the key measurement of the strain in semiconductors can be achieved using Raman spectroscopy.

The mechanical deformation affects significantly the PL emission, the nonuniformity in valley splitting, or the overlap of

C. L. Manganelli, I. Zaitsev, W. M. Klesse, D. Spirito  
IHP–Leibniz-Institut für innovative Mikroelektronik  
Im Technologiepark 25, 15236 Frankfurt (Oder), Germany  
E-mail: manganelli@ihp-microelectronics.com


M. Virgilio  
Dipartimento di Fisica “Enrico Fermi”  
Università di Pisa  
Largo Bruno Pontecorvo 3, 56127 Pisa, Italy

M. Montanari  
Dipartimento di Scienze  
Università degli Studi Roma Tre  
Viale G. Marconi 446, I-00146 Roma, Italy

N. Andriolli  
National Research Council of Italy (CNR-IEIT)  
56122 Pisa, Italy

S. Faralli  
Scuola Superiore Sant’Anna  
Istituto TECIP  
Via G. Moruzzi 1, 56127 Pisa, Italy

S. Tirelli, F. Dagnano  
Inphotec Fondazione  
Via G. Moruzzi 1, 56127 Pisa, Italy

 The ORCID identification number(s) for the author(s) of this article can be found under <https://doi.org/10.1002/pssa.202100293>.

© 2021 The Authors. physica status solidi (a) applications and materials science published by Wiley-VCH GmbH. This is an open access article under the terms of the Creative Commons Attribution-NonCommercial License, which permits use, distribution and reproduction in any medium, provided the original work is properly cited and is not used for commercial purposes.

DOI: 10.1002/pssa.202100293

electromagnetic modes with active device regions. Therefore, based on numerous available experimental results, approaches such as comparison between Raman, PL, and finite element method (FEM) calculations,<sup>[8,9]</sup> precession electron diffraction,<sup>[10]</sup> or electroluminescence<sup>[11]</sup> have been used for the interpretation of strain maps in Ge microstructures.

With the aim of developing a thorough guideline in the assessment and design of integrated light emitters, to be applied to Ge as well as GeSn, we have studied pure-Ge strained microstructures as a model system. We used numerical simulations that include the influence of mechanical and thermomechanical features on optical properties and Raman and PL experiments to benchmark the simulations.

In particular, we consider Ge micropillars with a silicon nitride (SiN) stressor layer deposited on top representing benchmark structures for both simulation and fabrication aspects. The mechanical deformation is calculated by a 3D FEM, disentangling mechanical and thermomechanical contributions, and evaluating the effect of the SiN stressor. Our study comprised the variation of strain on the surface and in the longitudinal (orthogonal to the surface) direction, together with the presence of nondiagonal strain components. The stressor-induced surface stress is compared with the experimental results obtained by means of micro-Raman spectroscopy.

Correspondingly, PL experiments allow assessing the strain-dependent band structure and the behavior of the strain field in the longitudinal direction. This includes the contribution of the thermal strain and the effect of the strain gradient, combined in a theoretical multivalley effective mass method.

This detailed analysis of temperature dependence on the valence band edges in strained Ge allows to revisit the direct gap behavior in relation to the carrier population of the valence band.<sup>[9]</sup>

## 2. Modeling Strain and Stress by Silicon Nitride with FEM and Comparison with Raman

The foundation of our theoretical analysis is the proper assessment of the mechanical (elastic) properties of 3D microstructures composed by Ge and SiN, where the latter acts as a stressor. These structures are fabricated as described in the following. The calculation uses a FEM simulation by inserting the elastic properties of the material to calculate the tensorial components of the strain.

To describe the deformation of semiconductors, the standard method is to make use of the Hooke's law,<sup>[12]</sup> i.e., the linear relation between strain and stress

$$\sigma_{ij} = C_{ijkl}\epsilon_{kl} \quad (1)$$

where  $\sigma_{ij}$  is the stress tensor,  $\epsilon_{kl}$  the strain tensor, and  $C_{ijkl}$  the tensor of stiffness.

The deformation of the germanium structures was computed using a 3D description in COMSOL Multiphysics assuming the stiffness constant  $C_{ijkl}$  of Equation (1), considering the orientation of the crystalline structure by means of the proper rotation of the elastic constant matrix and the nominal value of the silicon nitride stress.

The simulated structures were pillars of Ge on Si with a square cross section of 1.5, 3, or 5  $\mu\text{m}$  edge length ( $w$ ), with a height ( $h$ ) of 350 nm. On the top of the pillars, a SiN stressor applied a compressive stress of  $-1.8$  GPa, as shown in **Figure 1a**. These simulated structures were fabricated and experimentally investigated. The fabrication was conducted starting from an epitaxial Ge on Si substrate. On top of the Ge epilayer, the SiN stressor was formed first by depositing a 400 nm-thick layer by plasma-enhanced

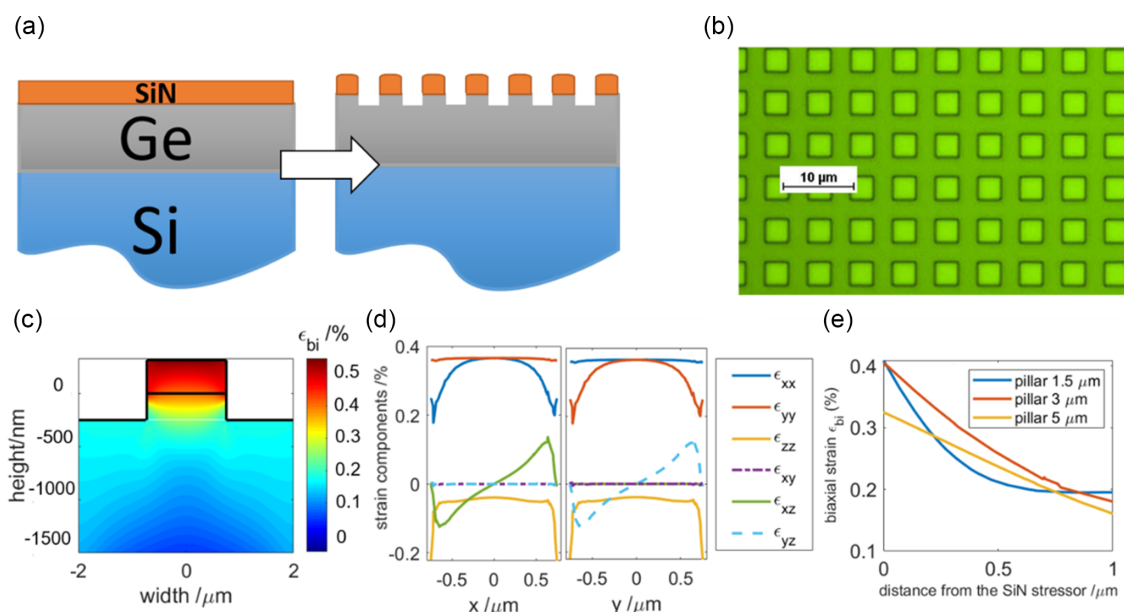


**Figure 1.** a) Scheme of the cross section of the pillars before and after patterning, b) optical microscopy image of the patterned pillars, c) simulated strain trace along the cross section of the pillar, d) the profile of all the strain components on an horizontal line 100 nm below the Ge/SiN interface evaluated in the  $xz$  plane (left) and  $yz$  plane (right), and e) the behavior of the strain profile as a function of the depth from the silicon nitride stressor for different size of the micropillar.

chemical vapor deposition (PECVD) using silane and ammonia as precursor gases. Deposition parameters such as gas fluxes, deposition pressure, RF power, and frequency were tuned to achieve the required stress of the deposited SiN layer. The stress was separately characterized by means of a mechanical profiler, which measured the bowing induced by the PECVD layer on a 6" Si wafer. After deposition of the SiN stress layer, the microstructures were obtained by patterning in regular arrays (Figure 1b) on a resist by e-beam lithography. The pattern was then transferred in the underlying layers with a fluorine-based dry etching process, removing the SiN in the exposed areas and etching down to  $h = 350$  nm inside the Ge layer (Figure 1a,c).

As an example of the fully coupled 3D FEM simulation, Figure 1c shows a cross section of a pillar of  $1.5 \mu\text{m}$  width with a color map of the biaxial strain  $\epsilon_{bi} = (\epsilon_{xx} + \epsilon_{yy})/2$ , with  $x$  and  $y$  indicating the in-plane directions. It can be seen that the maximum value of the biaxial strain in germanium is obtained at the interface between silicon nitride and germanium and it reaches a value of 0.4%.

To illustrate the behavior of the strain components, Figure 1d shows a profile of the strain components at a depth of 100 nm below the stressor in both the  $xz$  plane (left) and  $yz$  plane (right).

The structures under investigation present a  $90^\circ$  rotation invariance with respect to the axis normal to the growth direction ( $z$ ). As a direct consequence, the strain component  $\epsilon_{xx}$  in the  $xz$  plane shows the same behavior of the component  $\epsilon_{yy}$  in the  $yz$  plane, and correspondingly the  $\epsilon_{xx}$  in the  $yz$  plane shows the same behavior of the component  $\epsilon_{yy}$  in the  $xz$  plane. The strain component  $\epsilon_{zz}$  has a negative value, being bounded to the opposite of the ratio between the elastic constants ( $\epsilon_{zz} = -2 \frac{c_{12}}{c_{11}} \epsilon_{bi}$ ). The strain component  $\epsilon_{xy}$  is vanishing, while  $\epsilon_{xz}$  and  $\epsilon_{yz}$  can have non-negligible contributions, respectively, visible in the  $xz$  and  $yz$  plane.

As a direct consequence of Hooke's law in the hypothesis of absence of internal forces,<sup>[13]</sup> the diagonal components are symmetric with respect to the  $x$ -axis, while the nondiagonal components are antisymmetric ( $\epsilon_{ij}(x) = -\epsilon_{ij}(-x)$  (for  $i \neq j$ )).

The behavior of the biaxial strain as a function of the distance from the stressor is reported in Figure 1e for different size of the pillar, and shows a larger strain gradient for smaller structures.

The largest structure has a smaller strain at the interface and a smaller strain gradient. The  $1.5$  and  $3 \mu\text{m}$  squares have a similar strain at the interface, but the smallest structures have a large strain gradient up to  $0.5 \mu\text{m}$  of depth, and then the strain is almost constant. This difference in the depth range of the strain is relevant when combined with the penetration depth of the PL experiment (discussed in the following), and has to be taken into account in the design of microstructures for devices.

The experimental validation of FEM calculations was conducted using Raman spectroscopy, a widely available technique to gain information about strain and composition in semiconductors. In these experiments, we used an excitation wavelength of 532 nm, corresponding to a sampling depth of  $\approx 10$  nm in Ge (the SiN being transparent), i.e., we can use this technique to measure the strain at the Ge surface, where the effects of the stressor are stronger. Raman experiments were performed using a Renishaw inVia system, equipped with a spectrometer featuring a grating with  $1800 \text{ grooves mm}^{-1}$ . The setup operated in backscattering configuration. A Linkam liquid-nitrogen cryostat was used to control the temperature of the sample in the range 98–323 K. A long working distance objective ( $50\times$ ,  $0.5 \text{ NA}$ ) was used ( $\approx 900 \text{ nm}$  spot diameter).

In strained semiconductors, the phonon modes probed by Raman spectroscopy are shifted, with respect to the unstrained frequency  $\omega_0$  because of the deformation of the crystal lattice. The derivation of the strain-induced shift was widely discussed in previous studies<sup>[14–16]</sup> in the hypothesis of a bulk semiconductor. In this work, as in the case of Süess et al.,<sup>[17]</sup> we extended the analysis to a more complex geometry including 3D strain distribution, as shown above in Figure 1c–d. Therefore, we calculate the expected Raman shift measured on the surface of the sample and compare it directly with the experimental results, as shown in Figure 2. Considering the spatial resolution of the microscope and the edge effect of the structure, we take the off-diagonal strain components as negligible. With this assumption, we

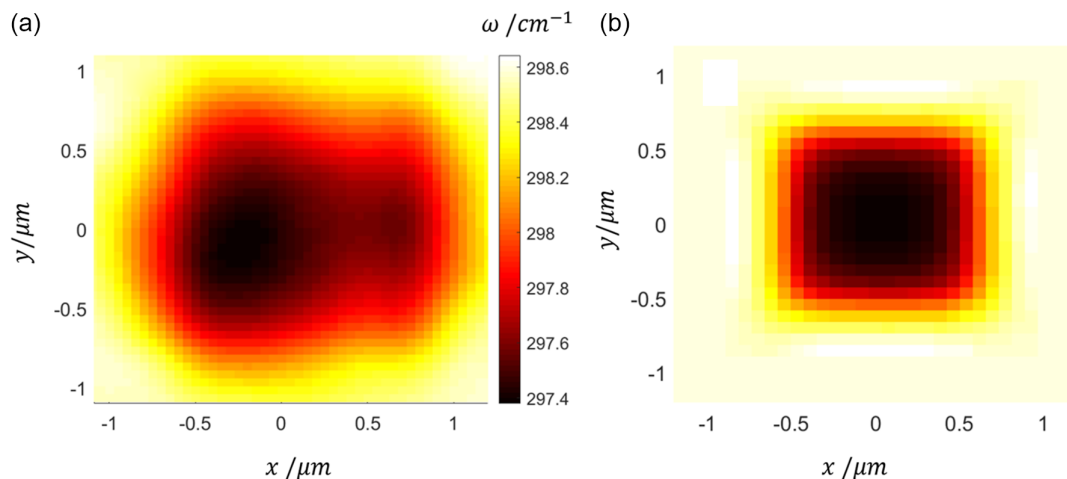


**Figure 2.** a) Experimental map of the Raman peak energy  $\omega$  for the square of  $1.5 \mu\text{m}$  and b) theoretical obtained by means of FEM calculations. The color scale is the same for the two maps.

calculate Raman shift for a fully biaxially strained structure, in back-scattering configuration, over the surface. The strain-induced Raman shift for the LO mode ( $\Delta\omega$ ) is proportional to  $p\varepsilon_{zz} + q(\varepsilon_{xx} + \varepsilon_{yy})$ , where  $p$  and  $q$  are the phonon deformation potentials and  $\varepsilon_{xx}$ ,  $\varepsilon_{yy}$ ,  $\varepsilon_{zz}$  the diagonal strain components.<sup>[18]</sup>

The simulated map in Figure 2 was obtained as  $\omega_0 + \Delta\omega$  by choosing the frequency  $\omega_0$  from the Raman map, in the area outside the SiN strained pillar, being equal to  $298.6 \text{ cm}^{-1}$ . From the comparison between the experimental data and the simulated strain, we extracted the values of the phonon deformation potentials  $p$  and  $q$  as  $p = 0.18 \omega_0^2$  and  $q = -1 \omega_0^2$ , in good agreement with previous studies.<sup>[19]</sup>

The analysis of Raman maps has also been performed at different temperatures. However, because of the limited penetration depth, these measurements give experimental evidence only for the strain at the surface of the Ge, and are not sufficient to assess the strain in the whole microstructures. To this aim, we use PL to study at the same time the band structure of the material and the effect of strain on it, as well as the interplay of strain and temperature, using a pump laser at 1064 nm, with a penetration depth of around 5  $\mu\text{m}$ .

### 3. Effect of Strain Gradient on PL Spectra

We have investigated the spatially resolved PL on the pillars as a function of temperature. Microphotoluminescence ( $\mu\text{PL}$ ) spectra were acquired in backscattering geometry using a 1064 nm laser pump focused on a spot of 1  $\mu\text{m}$  in diameter by a 50 $\times$  objective with a numerical aperture of 0.65. The pump excitation density is  $10^6 \text{ W cm}^{-2}$ . The emitted light was analyzed through a spectrometer and detected by an

extended-InGaAs photodiode array. The sample lattice temperature was controlled through a Linkam cryostat in the 100–430 K range within 5 K accuracy. In Figure 3a we report the experimental spectra obtained at different temperatures and for different positions of the laser spot. In the area outside the pillar, only thermal strain, arising from the difference between the coefficients of thermal expansion of Si and Ge,<sup>[20]</sup> is playing a role. In the inner area of the pillar, the contribution of mechanical deformation is also effective. Comparing the spectra from outer area and inner area (respectively continuous and dashed lines), we can observe that the main influence of the stressor layer is not on the peak position but on the lineshape that appears to be broader in the inner area of the pillar. For all the temperatures under investigation, the PL spectra indicate the quasi-direct nature of the Ge gap, showing the most intense peak at 0.85 eV for 113 K, 0.79 eV for 323 K, and 0.75 eV for 423 K, thus corresponding to radiative recombination across the direct gap.

The lineshape of these spectra exhibits a typical tail at high energy, related to the thermal distribution of carriers with a temperature  $T_e$  (the electronic temperature), which can be different from the lattice temperature  $T_L$  (assumed to be the nominal temperature) because of the nonequilibrium condition under light excitation. The actual value of  $T_e$  is an important input parameter for the full PL simulation.

Thus, the experimental PL spectra had been analyzed with the van Roosbroeck lineshape, previously applied to unstrained semiconductors.<sup>[21]</sup> We extended this procedure to the case of strained materials, where the deconvolution of the contributions of HH and LH valence bands is critical for the interpretation of the PL experiments and a proper evaluation of the parameters of the full model.<sup>[7]</sup>

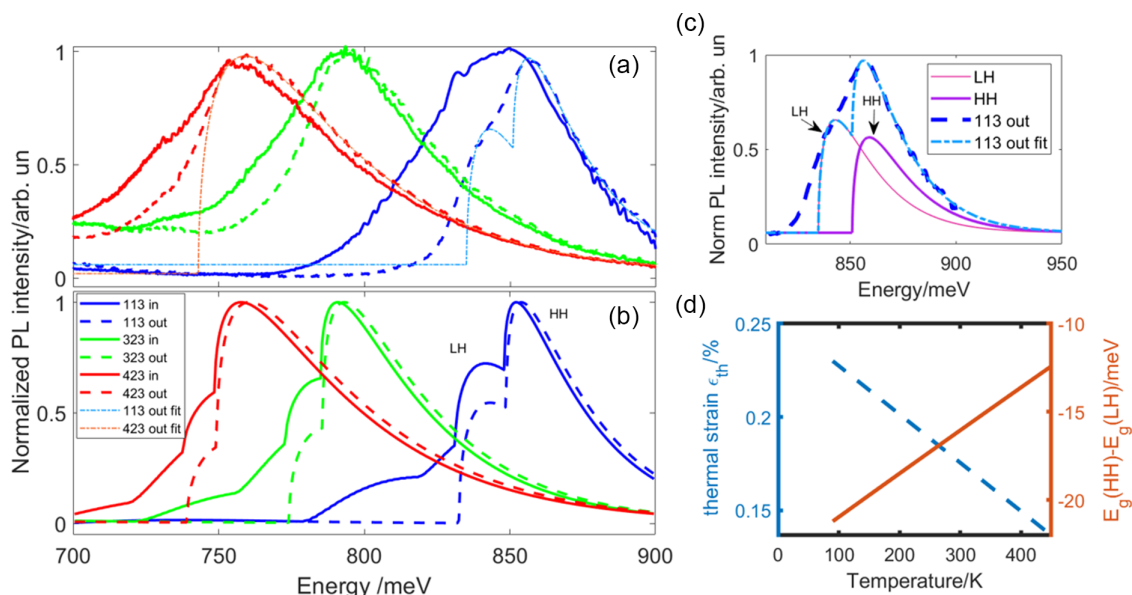


**Figure 3.** a) Experimental and b) calculated PL spectra in the inner (solid) and outer (dashed) part of the pillar. The orange and blue dash-dotted curves show the fit obtained with van Roosbroeck lineshape, respectively, for high and low temperatures. c) Experimental PL spectra at  $T = 113 \text{ K}$  (blue dashed curve), fit obtained following the approach of Equation (2) (light blue dot-dashed curve), single contribution of LH and HH bands to the fit (respectively pink and violet solid curves). d) Thermal strain<sup>[20]</sup> (blue dashed line, left axis) and the difference in energy between the direct gaps of HH and LH (red solid line, right axis) as a function of temperature.



By means of the approach of Van de Walle,<sup>[22]</sup> the offset for valence and conduction bands can be estimated as a function of strain. Considering the thermal strain  $\varepsilon_{th}(T)$ <sup>[20]</sup> (blue line of Figure 3d), the difference in energy between the direct gap for heavy hole ( $E_g(HH)$ ) and light hole ( $E_g(LH)$ ) varies between 12 and 20 meV in the investigated temperature range (orange line of Figure 3d), in good agreement with the results in Montanari et al.<sup>[23]</sup>

This represents an additional constraint in the van Roosbroeck fit that describes the recombination rate as a function of the thermal occupation number of the two bands  $\left(e^{-\frac{E-E_g(LH, HH)}{kT_e}}\right)$  and of the joint density of states  $\left(\sqrt{E-E_g(LH, HH)}\right)$

$$R = A_{HH} \sqrt{E-E_g(HH)} e^{-\frac{E-E_g(HH)}{kT_e}} + A_{LH} \sqrt{E-E_g(LH)} e^{-\frac{E-E_g(LH)}{kT_e}} \quad (2)$$

In this formula, the electronic temperature  $T_e$  is the same for both the bands and the other free parameters are the amplitude  $A_{HH}$  and  $A_{LH}$  and the energy gaps  $E_g(HH)$  and  $E_g(LH)$ .

The dot-dashed curves in Figure 3a show the results of the fit obtained with Equation 2. At low temperatures (blue dot-dashed curve), after having tagged the highest energy peak  $E_g(HH)$ , the value of the lowest energy one ( $E_g(LH)$ ) is constrained by the energy difference shown in Figure 3d. These two components are additionally shown in Figure 3c (LH, pink curve, HH, magenta curve) together with the complete fit (light blue dot-dashed curve). At higher temperatures (orange dot-dashed curve), the HH contribution plays a dominant role due to the higher population density, leading to the approximation  $A_{LH} \ll A_{HH}$ , in Equation (2).

The resulting  $T_e$  is higher than  $T_L$ , indicating heating of the carriers, for example, at  $T_L = 93$  K, we extract  $T_e = 162$  K. We highlight that the same analysis with a single band approach (i.e., with a single component in the van Roosbroeck function) would have led to an overestimation of the electronic temperature of more than 50 K.

The  $T_e$  obtained with the fit of Equation (2) and  $T_L$  are used in a multivalley effective mass model<sup>[7]</sup> to reproduce the PL spectra. This model considers both direct and indirect energy-resolved electron-hole recombination rates, estimated with first- and second-order perturbation theory, respectively.<sup>[7]</sup> These recombination rates are spatially resolved quantities controlled by quasi-Fermi levels in valence and conduction bands, and the model includes their dependence on doping, temperature, strain field, and excitation density, as well as self-absorption effects of the emitted photons in proximity of the external surface. The strain effects on the band edges are considered within the deformation potential theory; considering also the strain influence on the band curvatures, carrier distributions, and the dipole matrix elements. The model also includes energy and spatial dependent self-absorption effects as a function of power intensity as described in more detail in Virgilio et al.<sup>[24]</sup>

Moreover, we extend the model with the effect of strain non-uniformity along the vertical direction. We also exploit the temperature-dependent strain measured in an unpatterned Ge layer<sup>[20]</sup> for the outer part of the pillar, and the strain gradient

of Figure 1e for the inner part of the pillar to calculate the PL spectra from different parts of the sample. The distribution of the excess carrier density along the  $z$  direction is assumed to be temperature-dependent and the diffusion length of the excess carriers range from 5 to 1  $\mu\text{m}$  for temperatures from 91 to 400 K. The calculated carrier distribution shows a spatial dependence.<sup>[24]</sup> The maximum of excess carrier for the pump power under investigation ( $10^6 \text{ W cm}^{-2}$ ) is of  $10^{17}$  and  $6 \times 10^{12} \text{ cm}^{-3}$ , respectively, for  $\Gamma$  and L bands at 100 K and  $1.5 \times 10^{18}$  and  $10^{15} \text{ cm}^{-3}$  at 400 K. As also confirmed by the previous study in Virgilio et al.,<sup>[24]</sup> the maximum of excess carrier range from  $10^{15}$  to  $10^{18} \text{ cm}^{-3}$  for pump powers between  $10^2$  and  $10^6 \text{ W cm}^{-2}$ . The results of the model are shown in Figure 3b. The good agreement between theoretical and experimental data confirms the peak position, the blueshift, and broadening of the spectra from the outer area of the pillar with respect to those from the inner area. This effect is due to the nonuniform strain contribution induced by the SiN layer that is lowering the HH band in the inner area of the pillar. Moreover, increasing the tensile strain, the energy difference between LH and HH is increased and the LH band appears to be more populated and more effective in the electron-hole recombination, as shown in the tags of LH and HH of Figure 3b. Our theoretical and experimental results highlight the relevance of the strain gradient in the longitudinal direction, which is then an interesting tool for the proper design of Ge or GeSn microstructures in view of lasing applications.

### 3.1. Comparison with Varshni law

Apart from the effect of the temperature-dependent strain, the bandgap is intrinsically dependent on temperature. This is empirically modeled by the Varshni law,<sup>[25]</sup> whose coefficient for bulk Ge is well known. It is therefore interesting to verify if this law holds or is modified for the case of strained Ge, using our experimental data.

The normalized PL spectra are reported as a function of temperature and energy in the contour plot of Figure 4a.

For low temperatures, we can distinguish the two peaks, as shown in Figure 3a; at higher temperatures, the HH contribution is dominating the spectrum because of the higher occupation density. Figure 4 in the panels (b) and (c) shows the behavior of the energy gap, calculated from the fitting procedure described earlier, as a function of the estimated electronic temperature for both the bands. The Varshni formula reads

$$E_g = E_g(0) - \frac{\alpha T^2}{\beta + T} \quad (3)$$

where  $E_g(0)$  is the gap at  $T = 0$ ,  $\alpha$  is a coefficient related to the thermal expansion coefficient, and  $\beta$  is a term connected to the phonon interaction. We can assume that  $E_g(0)$  is mainly influenced by the strain, keeping a difference between HH and LH of 20 meV.

Analyzing separately the temperature dependence of HH and LH peaks, respectively, in Figure 4b,c and Table 1, we can observe how  $\beta$  is perfectly matching ( $\beta(HH) = \beta(LH)$ ) but the coefficient  $\alpha$  is higher in the case of HH. Considering the fact that the perfect disentanglement of the two bands is not straightforward at high temperature, we also present a fit procedure that

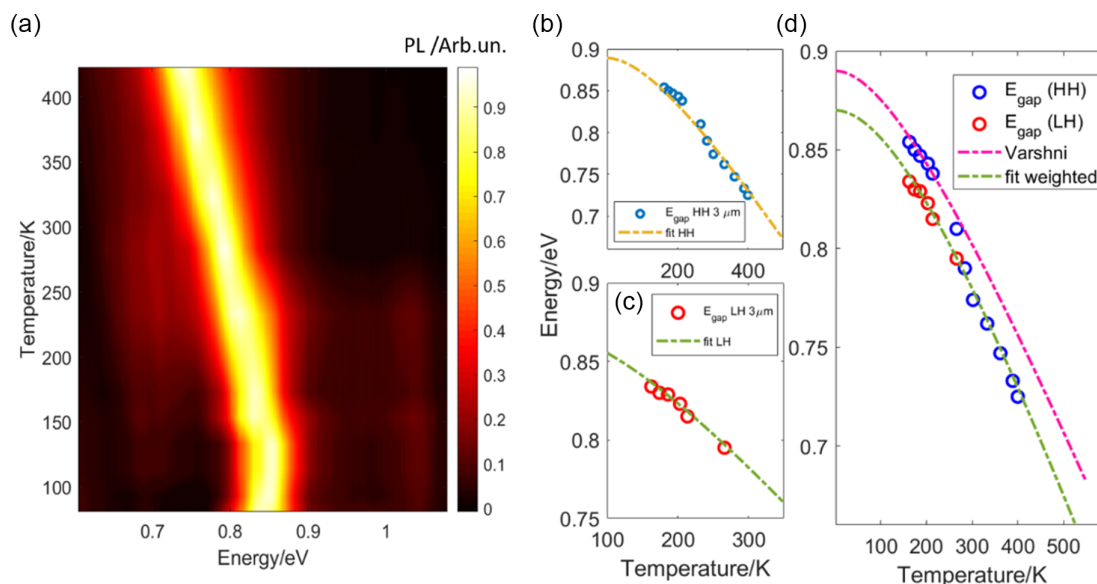


**Figure 4.** a) Contour plot of the normalized PL intensity as a function of the nominal temperature and the energy. b) Energy gap for HH band as a function of temperature for the geometry configuration of 3  $\mu\text{m}$ ; similar behavior is obtained for the geometry of 5  $\mu\text{m}$ . c) Energy gap for LH band as a function of temperature for the geometry configuration of 3  $\mu\text{m}$ ; similar behavior is obtained for the geometry of 5  $\mu\text{m}$ . d) Temperature dependence of the energy gap. Behavior of the HH band (blue circles), of the LH band (red circle), Varshni rule (magenta dot-dashed line), fit of the energy gap weighting on bands: LH for low temperatures and HH for high temperatures (green dashed line).

**Table 1.** Values of the fit parameters of obtained by fitting Equation (3) to temperature-dependent PL peak positions calculated with the fitting procedure using Equation (2).

Model	$E_g(0)$ [eV]	$\alpha$ [ $10^{-4}$ eV $\text{K}^{-1}$ ]	$\beta$ [K]
HH	0.889	6.9	296
LH	0.87	5.8	296
Varshni <sup>[25]</sup>	0.889	6.84	398
Fit weighted	0.87	7	398

couples the values extracted at low temperature for LH and the ones extracted at high temperature for HH, weighted by the relative carrier population (labeled “Fit weighted” in both Figure 4d and Table 1).  $\alpha$  and  $\beta$  are in perfect agreement with Varshni values, leading to the conclusion that a cumulative description of the energy gap as a function of temperature needs to be investigated in view of the weighted contributions of the two different bands.

## 4. Conclusions

In this work, we presented a combined theoretical–experimental approach to study the thermomechanical properties and the band structure of strained Ge microstructures.

The mechanical deformation is described in terms of a 3D FEM calculation including a SiN stressor and evaluating the surface and longitudinal effects of strain, together with the presence of nondiagonal components. The strain gradient profile, obtained by mechanical simulations, and the electronic and lattice temperatures, extracted from the experimental data, have been inserted in multivalley band structure calculation.

The combination of FEM and multivalley calculations developed in this work gives a clear interpretation of the PL data, describing not only the peak shift as a function of the temperature (Varshni rule), but also the strain-dependent broadening and the proper identification of the spectral features to the LH and HH bands.

Our approach allows to discriminate the impact evaluation of the effect of pure thermomechanical effects from temperature-determined band carrier occupation, which is critical in application to optoelectronic devices operating in a wide temperature range.

In perspective, our comprehensive approach can be applied to the design and characterization of strain-based electronic and optoelectronic devices, giving a quantitative description of the temperature-dependent strain relaxation mechanism and of the impact of local heating on the optical performance. These results can be beneficial also in the case of SiGeSn allows, and can find immediate use in more complex geometries, such as those used for lasing application.

## Supporting Information

Supporting Information is available from the Wiley Online Library or from the author.

## Acknowledgements

The authors acknowledge Prof. Giovanni Capellini for the fruitful discussion. C.L.M. acknowledges also Dr. Paolo Pintus for the wise suggestions and Chiara Fiore for the graphical support. M.M. acknowledges support by the European Union research and innovation program Horizon 2020 under the program “FLASH,” grant no. 766719.

Open access funding enabled and organized by Projekt DEAL.

## Conflict of interest

The authors declare no conflict of interest.

## Data Availability Statement

Research data are not shared.

## Keywords

germanium, photoluminescence, Raman, semiconductor, strain

Received: May 15, 2021

Revised: August 19, 2021

Published online: September 27, 2021

- [1] R. S. Jacobsen, K. N. Andersen, P. I. Borel, J. Fage-Pedersen, L. H. Frandsen, O. Hansen, M. Kristensen, A. V. Lavrinenko, G. Moulin, H. Ou, C. Peucheret, B. Zsigri, A. Bjarklev, *Nature* **2006**, 441, 199.
- [2] M. Cazzanelli, F. Bianco, E. Borga, G. Pucker, M. Ghulinyan, E. Degoli, E. Luppi, V. Vénard, S. Ossicini, D. Modotto, S. Wabnitz, R. Pierobon, L. Pavesi, *Nat. Mater.* **2012**, 11, 148.
- [3] C. L. Manganelli, P. Pintus, C. Bonati, *Opt. Express* **2015**, 23, 28649.
- [4] D. Stange, S. Wirths, R. Geiger, C. Schulte-Braucks, B. Marzban, N. von den Driesch, G. Mussler, T. Zabel, T. Stoica, J.-M. Hartmann, S. Mantl, Z. Ikonik, D. Grützmacher, H. Sigg, J. Witzens, D. Buca, *ACS Photonics* **2016**, 3, 1279.
- [5] O. Skibitzki, M. H. Zoellner, F. Rovaris, M. A. Schubert, Y. Yamamoto, L. Persichetti, L. Di Gaspare, M. De Seta, R. Gatti, F. Montalenti, G. Capellini, *Phys. Rev. Mater.* **2020**, 4, 103403.
- [6] G. Capellini, C. Reich, S. Guha, Y. Yamamoto, M. Lisker, M. Virgilio, A. Ghrib, M. El Kurdi, P. Boucaud, B. Tillack, T. Schroeder, *Opt. Express* **2014**, 22, 399.
- [7] M. Virgilio, C. L. Manganelli, G. Grosso, G. Pizzi, G. Capellini, *Phys. Rev. B* **2013**, 87, 235313.
- [8] A. Ghrib, M. El Kurdi, M. Prost, S. Sauvage, X. Checoury, G. Beaudoin, M. Chaigneau, R. Ossikovski, I. Sagnes, P. Boucaud, *Adv. Opt. Mater.* **2015**, 3, 353.
- [9] A. Ghrib, M. El Kurdi, M. de Kersauson, M. Prost, S. Sauvage, X. Checoury, G. Beaudoin, I. Sagnes, P. Boucaud, *Appl. Phys. Lett.* **2013**, 102, 221112.
- [10] A. Bashir, R. W. Millar, K. Gallacher, D. J. Paul, A. D. Darbal, R. Stroud, A. Ballabio, J. Frigerio, G. Isella, I. MacLaren, *J. Appl. Phys.* **2019**, 126, 155101.
- [11] M. Prost, M. El Kurdi, A. Ghrib, S. Sauvage, X. Checoury, N. Zerounian, F. Aniel, G. Beaudoin, I. Sagnes, F. Boeuf, P. Boucaud, *Opt. Express* **2015**, 23, 6722.
- [12] R. Camattari, L. Lanzoni, V. Bellucci, V. Guidi, *J. Appl. Crystallogr.* **2015**, 48, 943.
- [13] S. C. Jain, A. H. Harker, A. Atkinson, K. Pinardi, *J. Appl. Phys.* **1995**, 78, 1630.
- [14] R. Loudon, *Adv. Phys.* **1964**, 13, 423.
- [15] S. Ganesan, A. A. Maradudin, J. Oitmaa, *Ann. Phys.* **1970**, 56, 556.
- [16] E. Anastassakis, *J. Appl. Phys.* **1997**, 81, 3046.
- [17] M. J. Süess, R. A. Minamisawa, R. Geiger, K. K. Bourdelle, H. Sigg, R. Spolenak, *Nano Lett.* **2014**, 14, 1249.
- [18] E. Anastassakis, M. Cardona, in *Semiconductors and Semimetals*, Vol. 55 (Eds: T. Suski, W. Paul), Elsevier, Amsterdam **1998**, pp. 117–233.
- [19] A. Gassenq, S. Tardif, K. Guillo, I. Duchemin, N. Pauc, J. M. Hartmann, D. Rouchon, J. Widiez, Y. M. Niquet, L. Milord, T. Zabel, H. Sigg, J. Faist, A. Chelnokov, F. Rieutord, V. Reboud, V. Calvo, *J. Appl. Phys.* **2017**, 121, 055702.
- [20] C. L. Manganelli, M. Virgilio, O. Skibitzki, M. Salvalaglio, D. Spirito, P. Zaumseil, Y. Yamamoto, M. Montanari, W. M. Klesse, G. Capellini, *J. Raman Spectrosc.* **2020**, 51, 989.
- [21] H. Barry Bebb, E. W. Williams, in *Semiconductors and Semimetals*, Vol. 8 (Eds: R. K. Williardson, A. C. Beer), Academic, New York **1972**, pp. 289–295.
- [22] C. G. Van de Walle, *Phys. Rev. B* **1989**, 39, 1871.
- [23] M. Montanari, M. Virgilio, C. L. Manganelli, P. Zaumseil, M. H. Zoellner, Y. Hou, M. A. Schubert, L. Persichetti, L. Di Gaspare, M. De Seta, E. Vitiello, E. Bonera, F. Pezzoli, G. Capellini, *Phys. Rev. B* **2018**, 98, 195310.
- [24] M. Virgilio, C. L. Manganelli, G. Grosso, T. Schroeder, G. Capellini, *J. Appl. Phys.* **2013**, 114, 243102.
- [25] Y. P. Varshni, *Physica* **1967**, 34, 149.